Monthly Notices of the ROYAL ASTRONOMICAL SOCIETY

MNRAS **498,** 3578–3591 (2020)
Advance Access publication 2020 August 27

doi:10.1093/mnras/staa2622

Long-term optical and infrared variability characteristics of Fermi blazars

P. Z. Safna,[1]★ C. S. Stalin [2]★ Suvendu Rakshit [3] and Blesson Mathew [1]

[1]*Department of Physics and Electronics, CHRIST (Deemed to be University), Hosur Road, Bangalore-560029, India*
[2]*Indian Institute of Astrophysics, Department of Science and Technology, Block II, Koramangala, Bangalore-560034, India*
[3]*Finnish Centre for Astronomy with ESO (FINCA), University of Turku, Quantum, FI-20014 Vesilinnantie 5, Finland*

Accepted 2020 August 25. Received 2020 August 25; in original form 2020 March 14

ABSTRACT

We present long-term optical and near-infrared flux variability analysis of 37 blazars detected in the γ-ray band by the *Fermi Gamma-Ray Space Telescope*. Among them, 30 are flat spectrum radio quasars (FSRQs) and 7 are BL Lac objects (BL Lacs). The photometric data in the optical (*BVR*) and infrared (*JK*) bands were from the Small and Moderate Aperture Research Telescope System acquired between 2008–2018. From cross-correlation analysis of the light curves at different wavelengths, we did not find significant time delays between variations at different wavelengths, except for three sources, namely PKS 1144–379, PKS B1424–418, and 3C 273. For the blazars with both *B*- and *J*-band data, we found that in a majority of FSRQs and BL Lacs, the amplitude of variability (σ_m) in the *J* band is larger than that in *B* band, consistent with the dominance of the non-thermal jet over the thermal accretion disc component. Considering FSRQs and BL Lacs as a sample, there are indications of σ_m to increase gradually towards longer wavelengths in both, however, found to be statistically significant only between *B* and *J* bands in FSRQs. In the $B - J$ v/s *J*-colour magnitude diagram, we noticed complicated spectral variability patterns. Most of the objects showed a redder when brighter (RWB) behaviour. Few objects showed a bluer when brighter (BWB) trend, while in some objects both BWB and RWB behaviours were noticed. These results on flux and colour characteristics indicate that the jet emission of FSRQs and BL Lacs is indistinguishable.

Key words: galaxies: active – BL Lacertae objects: general – galaxies: jets – galaxies: nuclei.

1 INTRODUCTION

Active Galactic Nuclei (AGNs) are actively accreting supermassive black holes (SMBHs) at the centres of massive galaxies (Antonucci 1984; Urry & Padovani 1995). The radiation from AGN is believed to result from the accretion of matter by the SMBH at the centre of its host galaxy (Lynden-Bell 1969; Rees 1984). Among AGN are the blazars that show large amplitude flux variations (Wagner & Witzel 1995; Ulrich, Maraschi & Urry 1997) over the entire accessible bands of the electromagnetic spectrum. The emission from blazars is dominated by non-thermal emission from their relativistic jets that are aligned close to the observer. They are broadly classified into two categories, namely flat spectrum radio quasars (FSRQs) and BL Lac objects (BL Lacs). This division is from an observational perspective and it is based on the presence of broad emission lines in their optical spectra with FSRQs having broad emission lines with equivalent width (EW) > 5 Å. On a more physical ground, it is now thought that FSRQs have radiatively efficient optically thick and geometrically thin accretion disc, while BL Lacs have radiatively inefficient accretion disc that cannot photoionize the line emitting clouds (Ghisellini & Celotti 2001; Ghisellini, Maraschi & Tavecchio 2009; Ghisellini 2019).

The broad-band spectral energy distribution (SED) of blazars shows a two hump structure. The low energy hump, extending from radio through X-rays is dominated by the optically thin synchrotron emission process by the energetic electrons in the jet (Konigl 1981; Urry & Mushotzky 1982). The radio/optical emission that contributes to this component of the SED is found to be highly polarized (Angel & Stockman 1980). The origin of the high energy hump that spans the X-ray and γ-ray region is not well-understood. In the leptonic scenario (Böttcher 2007), the high energy hump could be produced by inverse Compton scattering of seed photons by the same electrons in the jet that are responsible for the synchrotron emission (synchrotron self Compton; Jones, O'dell & Stein 1974) as well as photons that are exterior to the jet (external Compton; Dermer & Schlickeiser 1993; Sikora, Begelman & Rees 1994). However, the nature of the seed photons that take part in the inverse Compton process is poorly understood. Alternatively, in the hadronic scenario, the second hump could also be produced by synchrotron radiation from protons that are co-accelerated along with the jet electrons, interaction of relativistic protons with external radiation fields as well as proton induced particle cascades (Mücke & Protheroe 2001; Mücke et al. 2003). Clues to a better understanding of the emission processes in blazars can be attained by studying correlated flux variations between different spectral bands.

Blazars have been extensively studied for flux variability in multiple wavebands (Bonning et al. 2012; Rakshit et al. 2017; Rani, Stalin & Rakshit 2017; Liodakis et al. 2018; Meng et al. 2018), yet, we do not have a clear understanding of the cause of flux variations in them. In addition to flux variations, blazars also exhibit

★ E-mail: pzsafna@gmail.com (PZS); stalin@iiap.res.in (CSS)

Table 1. The sample of sources analysed for variability. The details of the sources are from Ackermann et al. (2015).

Name	α_{2000}	δ_{2000}	z	Type	SED type	MJD of observation	Filters
PMN J0017–0512	00:17:35.82	– 05:12:42	0.227	FSRQ	LSP	56442–57297	*B*,*V*,*R*,*J*,*K*
4C+01.02	01:08:38.76	01:34:60	2.090	FSRQ	LSP	56552–57960	*B*,*R*,*J*
AO 0235+164	02:38:38.93	16:36:59	0.940	BL Lac	LSP	54501–57265	*B*,*V*,*R*,*J*,*K*
PKS 0250–225	02:52:47.95	– 22:19:25	1.419	FSRQ	LSP	56247–56994	*B*,*V*,*R*,*J*,K
PKS 0301–243	03:03:26.50	– 24:07:11	0.260	BL Lac	HSP	56171–57093	*B*,*R*,*J*
PKS 0402–362	04:03:53.70	– 36:05:02	1.423	FSRQ	LSP	55838–57297	*B*,*V*,*R*,*J*,*K*
PKS 0426–380	04:28:40.42	– 37:56:20	1.111	BL Lac	LSP	56282–57791	*B*,*V*,*R*,*J*,*K*
PKS 0454–234	04:57:03.20	– 23:24:52	1.003	FSRQ	LSP	55861–57144	*B*,*V*,*R*,*J*,*K*
S3 0458–02	05:01:12.80	– 01:59:14	2.088	FSRQ	LSP	56192–57342	*B*,*R*,*J*,*K*
PKS 0502+049	05:05:23.18	04:59:43	0.954	FSRQ	LSP	56357–57129	*B*,*R*,*J*
PKS 0454–46	05:07:54.60	– 61:04:43	0.853	FSRQ	LSP	55488–57154	*B*,*R*,*J*
PKS 0528+134	05:30:56.36	13:31:55	2.070	FSRQ	LSP	54501–57095	*B*,*V*,*R*,*J*
PKS 0537–441	05:38:50.30	– 44:05:09	0.896	BL Lac	LSP	55590–57143	*B*,*R*,*J*,*K*
PKS 0637–75	06:35:46.50	– 75:16:17	0.653	FSRQ	LSP	55489–57152	*B*,*R*,*J*
0736+01	07:39:18.03	01:37:05	–	FSRQ	ISP	56986–57179	*B*,*R*,*J*
PKS 0805–077	08:08:15.50	– 07:51:10	1.837	FSRQ	LSP	56697–57186	*B*,*R*,*J*
BZQ J0850–1213	08:50:09.60	– 12:13:35	0.566	FSRQ	LSP	55496–57196	*B*,*R*,*J*
OJ 287	08:54:48.87	20:06:31	0.306	BL Lac	LSP	54501–57857	*B*,*V*,*R*,*J*,*K*
PKS 1004–217	10:06:46.40	– 21:59:20	0.331	FSRQ	ISP	55588–57185	*B*,*V*,*R*,*J*
1059–1134	10:59:12.43	– 11:34:23	–	BL Lac	LSP	55941–57180	*B*,*R*,*J*
PKS 1144–379	11:47:01.40	– 38:12:11	1.048	FSRQ	LSP	55590–57180	*B*,*V*,*R*,*J*,*K*
3C 273	12:29:06.69	02:03:09	0.158	FSRQ	LSP	54501–57856	*B*,*V*,*R*,*J*,*K*
PKS 1244–255	12:46:46.80	– 25:47:49	0.638	FSRQ	LSP	55599–57191	*B*,*R*,*J*
3C 279	12:56:11.10	– 05:47:22	0.536	FSRQ	LSP	54501–57953	*B*,*V*,*R*,*J*,*K*
PKS B1406–076	14:08:56.48	– 07:52:27	1.494	FSRQ	LSP	54501–57867	*B*,*V*,*R*,*J*,*K*
PKS B1424–418	14:27:56.30	– 42:06:19	1.522	FSRQ	LSP	55942–57915	*B*,*V*,*R*,*J*,*K*
PKS 1510–08	15:12:50.53	– 09:05:59	0.360	FSRQ	LSP	54501–57919	*B*,*V*,*R*,*J*,*K*
PKS 1622–29	16:26:06.02	– 29:51:27	0.185	FSRQ	LSP	54501–57150	*B*,*V*,*R*,*J*,*K*
PKS 1730–13	17:33:02.70	– 13:04:50	0.902	FSRQ	LSP	54501–57197	*B*,*V*,*R*,*J*,*K*
PKS 1954–388	19:57:59.80	– 38:45:06	0.630	FSRQ	LSP	55490–57341	*B*,*R*,*J*
2023–07	20:25:40.66	– 07:35:53	1.388	FSRQ	LSP	57270–57964	*B*,*R*,*J*
PKS 2052–47	20:56:16.30	– 47:14:48	1.489	FSRQ	LSP	55063–57187	*B*,*V*,*R*,*J*,*K*
PKS 2142–75	21:47:12.70	– 75:36:13	1.139	FSRQ	LSP	55296–57193	*B*,*V*,*R*,*J*,*K*
PKS 2155–304	21:58:52.07	– 30:13:32	0.117	BL Lac	HSP	54603–57964	*B*,*V*,*R*,*J*,*K*
3C 454.3	22:53:57.75	16:08:54	0.859	FSRQ	LSP	54640–57964	*B*,*V*,*R*,*J*,*K*
PKS 2326–502	23:29:20.88	– 49:55:41	0.518	FSRQ	LSP	56108–57200	*B*,*R*,*J*,*K*
PMN J2345–1555	23:45:12.46	– 15:55:08	0.621	FSRQ	LSP	55873–57200	*B*,*R*,*J*,*K*

spectral variations. Available observational results in literature point to complex spectral variability behaviours in them (Bonning et al. 2012; Meng et al. 2018; Rajput et al. 2019). Analysis of colour magnitude trends in monitoring data of blazars has revealed complex patterns such as bluer when brighter (BWB) trend (Stalin et al. 2009), redder when brighter (RWB) trend (Sarkar et al. 2019), both BWB and RWB trends (Rajput et al. 2019) and no/weak spectral change with brightness (Raiteri et al. 2003). To better understand the complex flux and spectral behaviour of blazars, it is important to analyse near simultaneous data on a large number of blazars that spans over many years. With this objective, we have carried out a systematic analysis of the photometric monitoring data on a total of 37 blazars to characterize their flux and spectral variability behaviour as well as correlations if any between flux variations between different wavelengths. The sample and data are described in Section 2. The analysis is discussed in Section 3. The results are discussed in Section 4 followed by the summary in the final section.

2 SAMPLE AND DATA

Our sample of sources for this study was selected from the list of blazars that are routinely monitored by the Small and Moderate Aperture Research Telescope System (SMARTS[1]; Bonning et al. 2012) in the optical and near-infrared bands. They are part of a list of γ-ray emitting blazars regularly monitored by SMARTS. First, we selected all objects from SMARTS and restricted our analysis to only those objects that satisfy the criteria of the availability of greater than 40 data points in at least any two optical bands and one infrared band during the period 2008–2018. This constraint leads us to a total of 37 blazars of which 30 are FSRQs and 7 are BL Lacs. For 19 sources in our sample, we have data in all the five photometric bands, namely *B*, *V*, *R*, *J*, and *K*. For two sources, we have data in *B*, *V*, *R,* and *J* bands. Data in three bands *B*, *R*, and *J* are available for 12 sources in our sample and the remaining 4 sources have data in four bands, namely *B*, *R*, *J,* and *K*. The details of the objects that were analysed for flux variations in this work are given in Table 1. From visual inspection of each of the light curves, we noticed few photometric points with large error bars. To avoid such points in the analysis of the light curves, we calculated the median of the photometric errors in each light curve and removed those points that have photometric errors larger than 10 times the median error. The final multiband light curves of the objects are given in Figs 1–4.

[1]http://www.astro.yale.edu/smarts/fermi

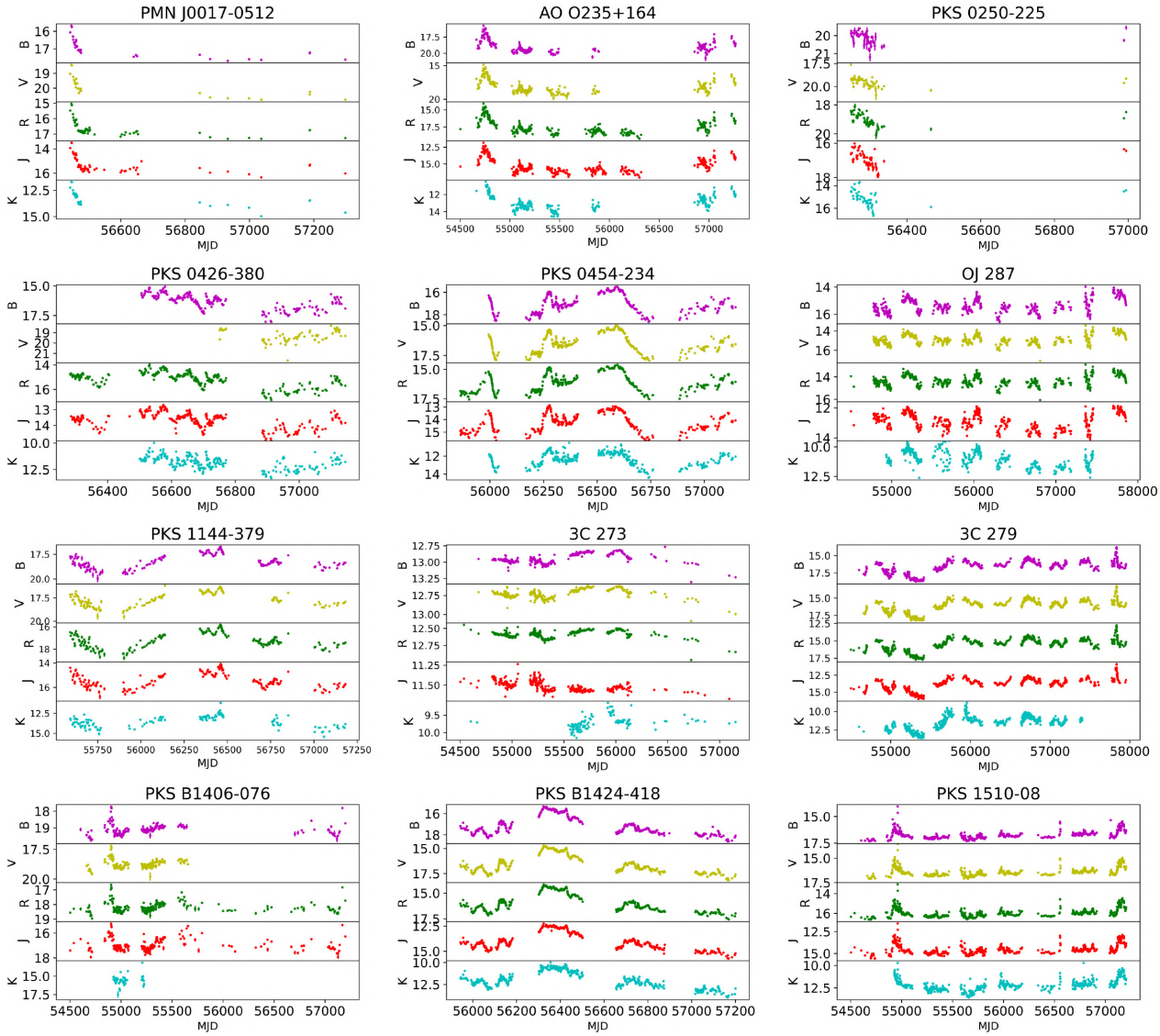

Figure 1. Multiwavelength light curves (magnitude v/s MJD) of the blazars studied in this work. Different colours represent different frequencies. *B* (violet), *V* (yellow), and *R* (green) are the optical bands and *J* (red) and *K* (blue) are the IR bands. The names of the objects are given on each panel.

3 ANALYSIS

3.1 Flux variability

To characterize the flux variability nature of the sources, we calculated the intrinsic amplitude of variability (σ_m) as outlined in Rakshit & Stalin (2017). The σ_m was calculated from the observed light curves after subtracting the errors in the photometric measurements as follows (see also Sesar et al. 2007)

$$\Sigma = \sqrt{\frac{1}{n-1}\sum_{i=1}^{N}(m_i - < m >)^2}, \quad (1)$$

where <m> is the weighted mean of the magnitude in each band and σ_m is given by,

$$\sigma_m = \begin{cases} \sqrt{\Sigma^2 - \epsilon^2} & \text{if } \Sigma \geq \epsilon, \\ 0, & \text{otherwise} \end{cases} \quad (2)$$

Σ^2 is the variance of the light curve and ϵ represents the errors in the photometric measurements and it is calculated directly from individual measurement errors ϵ_i as

$$\epsilon^2 = \frac{1}{N}\sum_{i=1}^{N}\epsilon_i^2. \quad (3)$$

The values of σ_m calculated for the sources along with the number of data points available in each band are given in Table 2. Considering individual objects, σ_m in the infrared *J* and *K* bands is larger than the optical *B* band for about 80 per cent of the objects. The mean σ_m values along with their standard deviations in different bands for FSRQ and BL Lac as a population are given in Table 3. From Table 3, there are indications that the average σ_m in the infrared *J* and *K* bands for the blazars studied here are larger than the optical bands for both the FSRQ and BL Lac population, with the trend of increasing σ_m towards longer wavelengths. However, given the large standard deviations to the mean σ_m given in Table 3, it is difficult to make a strong claim of σ_m increasing from shorter towards longer

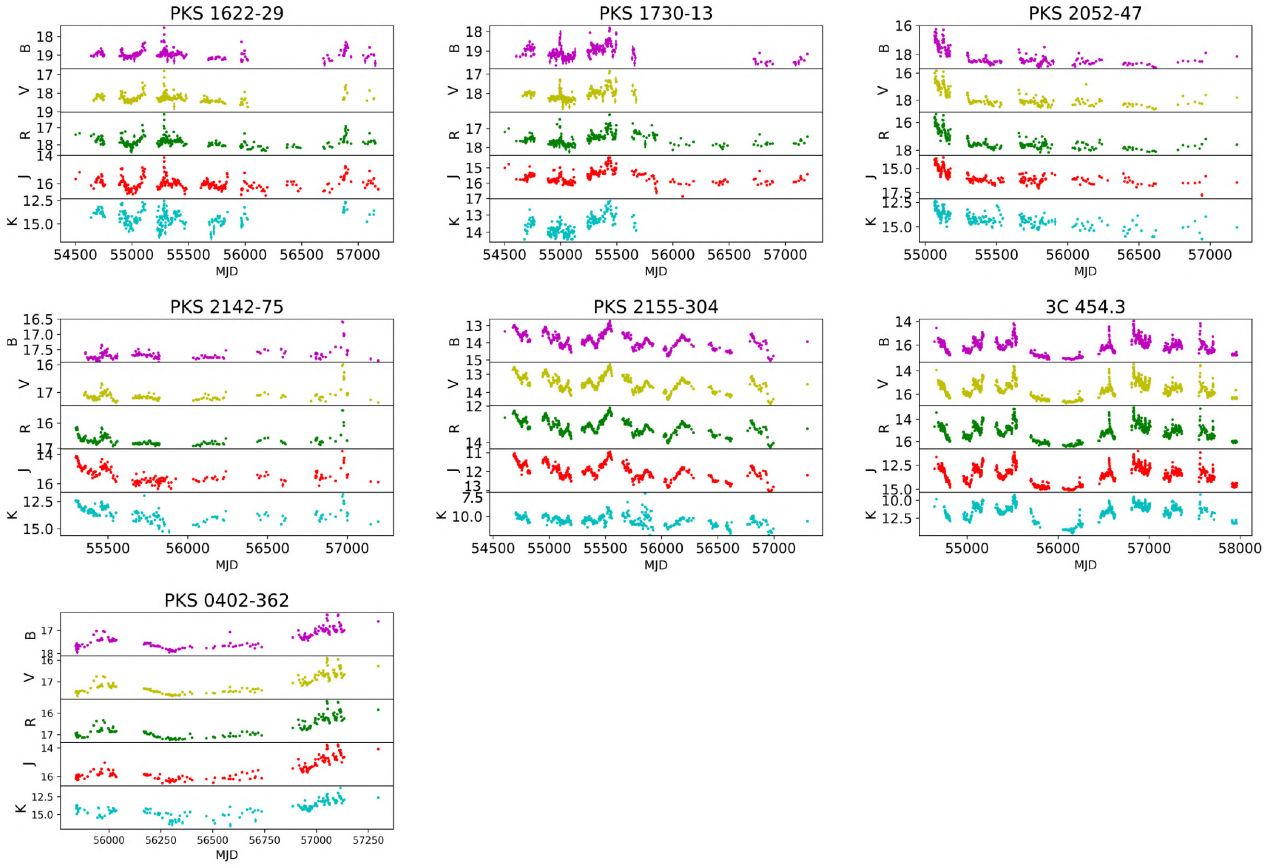

Figure 2. Multiwavelength light curves (magnitude v/s MJD) of the blazars studied in this work. Different colours represent different frequencies. *B* (violet), *V* (yellow), and *R* (green) are the optical bands and *J* (red) and *K* (blue) are the IR bands. The names of the objects are given on each panel.

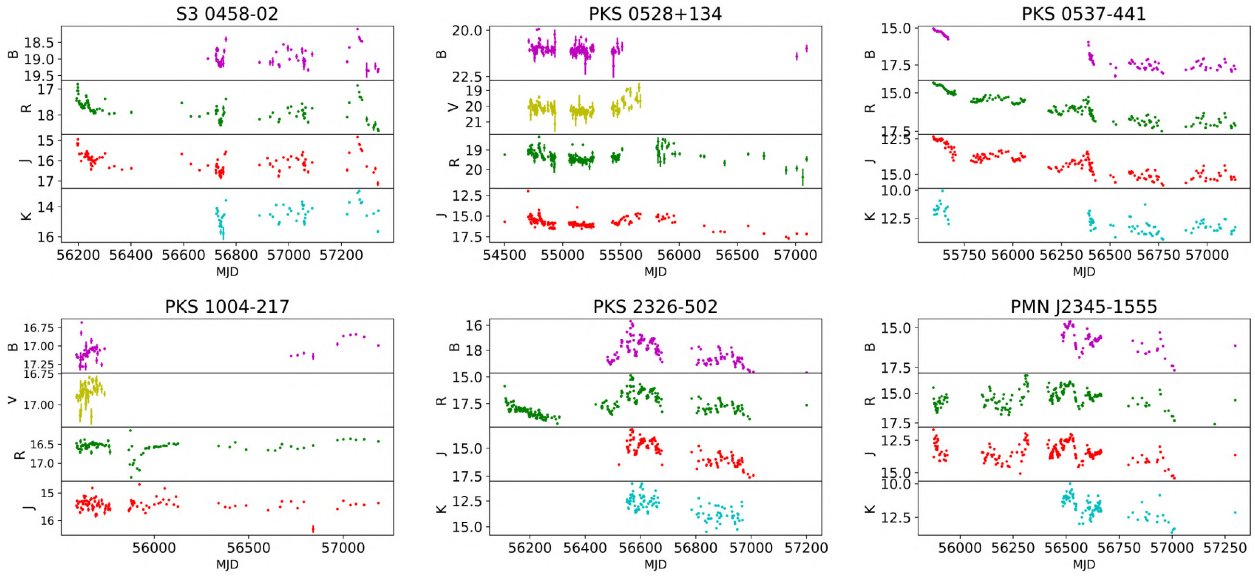

Figure 3. Multiwavelength light curves (magnitude v/s MJD) of the blazars. Different colours represent different frequencies. *B* (violet), *V* (yellow), and *R* (Green) are the optical bands and *J* (red) and *K* (blue) are the IR bands. The names of the objects are given on each panel.

wavelengths for both FSRQ and BL Lac population. To ascertain the difference in the mean σ_m between different wavelengths, we did a two sample Kolmogorov–Smironv (KS) test. We restricted this test to *B*, *R*, and *J* bands, due to the availability of σ_m measurements for all the sources in these bands. For BL Lacs, between *B* and *R* bands, we found a D statistics of 0.143 and a null hypothesis (no difference in σ_m between *B* and *R* bands) probability (*p*) of 1.00. Between *B* v/s *J* (*R* v/s *J*), we found D value of 0.286 (0.286) and null hypothesis

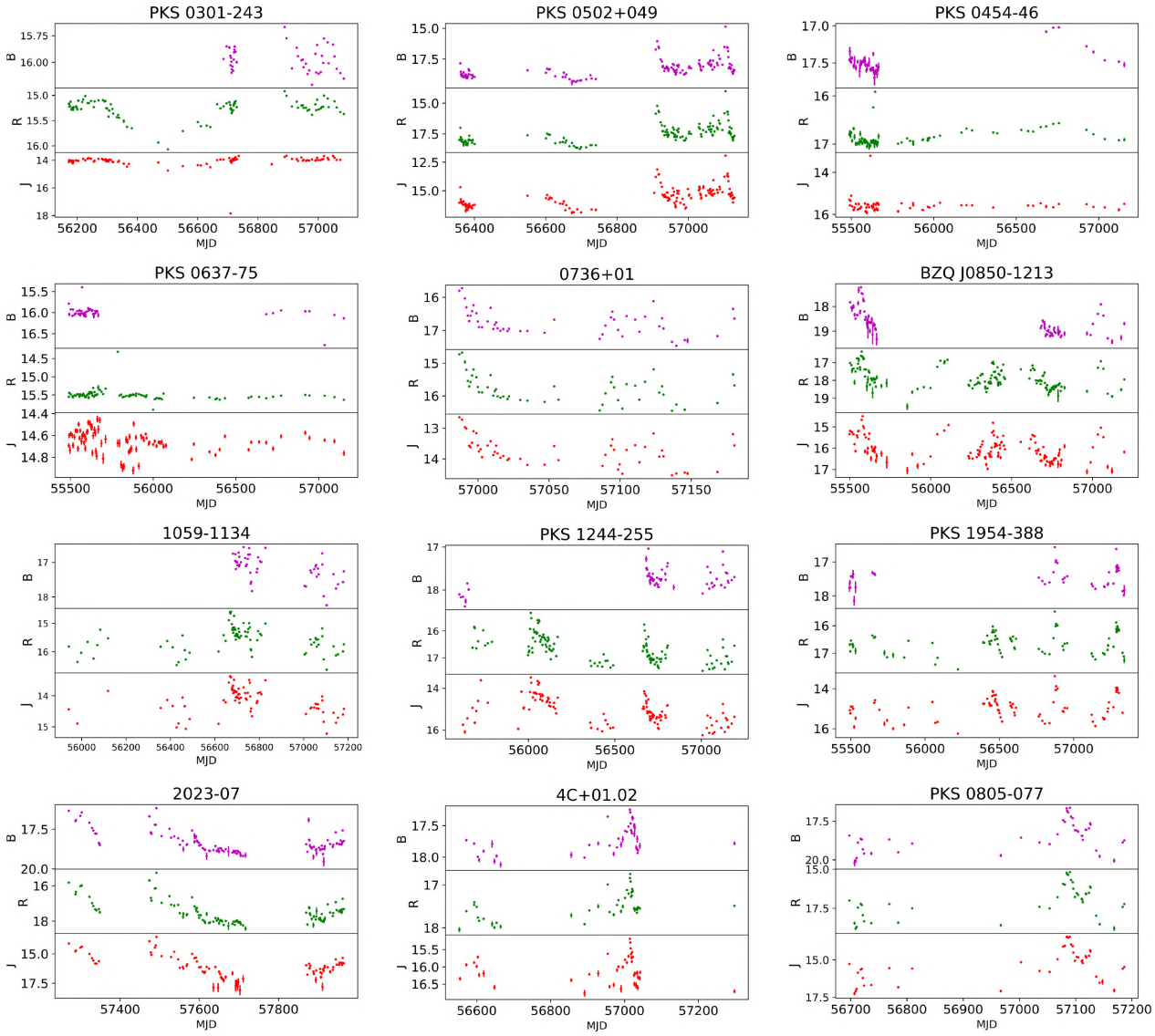

Figure 4. Multiwavelength light curves (magnitude v/s MJD) of the blazars studied in this work. Different colours represent different frequencies. *B* (violet), *V* (yellow), and *R* (Green) are the optical bands and *J* (red) and *K* (blue) are the IR bands. The names of the objects are given on each panel.

p value of 0.883 (0.883). Thus, for BL Lacs as a population, the observed hint of increased variability towards longer wavelengths is not statistically significant. Similarly, for FSRQs, between *B* and *R* bands, our KS test gave a D statistic of 0.167 and *p* of 0.760. For variations between *B* and *J* bands, we found a D value of 0.400 and a *p* of 0.011. And, between *R* and *J* bands, the obtained D and *p* values are 0.233 and 0.342, respectively. Thus, the two sample KS test conducted between the distributions of σ_m between *B* and *J* bands in FSRQs confirms that the two distributions are indeed different, and therefore, the difference in mean σ_m between *J* and *B* band is statistically significant. Also, the differences in the mean σ_m between (*B*,*R*) and (*R*,*J*) are statistically insignificant. Similarly in all the bands (except the *K* band), the mean σ_m in BL Lacs is larger than that of FSRQs (see Table 3). Here too, as the standard deviations are larger, we did a KS test. For *B* band, we found a D statistics and *p* value (null hypothesis probability of no difference in the σ_m between BL Lacs and FSRQs) of 0.324 and 0.504, respectively. Similarly, for *V* band (*R* band), we found D and *p* values of 0.412 (0.224) and 0.519 (0.901), respectively. For *J* band, we found a D and *p* of 0.314 and 0.543, while for K band, the D and p values are 0.289 and 0.834, respectively. Thus, from KS test, we found that the distribution of σ_m between FSRQs and BL Lacs in all the bands is indistinguishable. Analysis similar to the one carried out in this work is needed on a larger number of FSRQs and BL Lacs to confirm if BL Lacs indeed show σ_m larger than FSRQs on month to year like time-scales.

3.2 Colour variability

In addition to flux variations, blazars are also known to show spectral variations. The photometric measurements in *BVRJK* bands analysed here have contributions from both thermal emission coming from the accretion disc and non-thermal emission coming from the relativistic jet. Both these processes contribute differently to the emission in different bands. Thus, by studying spectral variations, one can distinguish the different components contributing to the observed flux variations. To characterize the nature of spectral variations in

Table 2. Results of the analysis of variability. The numbers in parenthesis are the number of data points corresponding to each band.

Name	*B*	*V*	*R*	*J*	*K*	Spectral variability	Type
PMN J0017–0512	0.498 (54)	0.617 (45)	0.528 (81)	0.675 (85)	0.699 (51)	RWB	FSRQ
4C+01.02	0.233 (42)	–	0.306 (44)	0.403 (42)	–	RWB	FSRQ
AO 0235+164	0.962 (221)	1.007 (239)	1.003 (301)	1.084 (333)	0.858 (238)	RWB,BWB	BL Lac
PKS 0250–225	0.346 (49)	0.500 (55)	0.547 (55)	0.442 (56)	0.664 (48)	RWB	FSRQ
PKS 0301–243	0.114 (46)	–	0.179 (97)	0.432 (93)	–	RWB	BL Lac
PKS 0402–362	0.370 (175)	0.412 (174)	0.425 (169)	0.666 (167)	1.036 (156)	RWB	FSRQ
PKS 0426–380	0.579 (372)	0.564 (73)	0.538 (480)	0.451 (482)	0.566 (384)	BWB	BL Lac
PKS 0454–234	0.788 (340)	0.761 (339)	0.765 (381)	0.703 (369)	0.714 (336)	BWB	FSRQ
S3 0458–02	0.283 (57)	–	0.357 (110)	0.427 (103)	0.626 (52)	RWB	FSRQ
PKS 0502+049	0.717 (131)	–	0.778 (131)	0.844 (135)	–	RWB	FSRQ
PKS 0454–46	0.148 (42)	–	0.182 (65)	0.345 (57)	–	RWB	FSRQ
PKS 0528+134	0.281 (117)	0.337 (146)	0.300 (186)	0.605 (207)	–	RWB	FSRQ
PKS 0537–441	0.967 (91)	–	0.791 (192)	0.851 (179)	0.851 (86)	RWB	BL Lac
PKS 0637–75	0.159 (45)	–	0.151 (85)	0.096 (88)	–	RWB	FSRQ
0736+01	0.377 (52)	–	0.412 (52)	0.452 (53)	–	RWB	FSRQ
PKS 0805–077	0.954 (43)	–	1.042 (42)	1.080 (44)	–	RWB	FSRQ
BZQ J0850–1213	0.522 (76)	–	0.571 (144)	0.564 (132)	–	RWB	FSRQ
OJ 287	0.522 (573)	0.507 (576)	0.476 (578)	0.535 (525)	0.665 (417)	RWB	BL Lac
PKS 1004–217	0.121 (53)	0.070 (42)	0.173 (98)	0.228 (93)	–	RWB	FSRQ
1059–1134	0.366 (52)	–	0.430 (83)	0.417 (79)	–	No trend	BL Lac
PKS 1144–379	0.692 (173)	0.743 (148)	0.662 (184)	0.591 (181)	0.705 (132)	No trend	FSRQ
3C 273	0.074 (316)	0.061 (318)	0.056 (325)	0.062 (306)	0.183 (121)	RWB	FSRQ
PKS 1244–255	0.261 (69)	–	0.501 (190)	0.677 (167)	–	RWB	FSRQ
3C 279	0.958 (778)	0.944 (771)	0.905 (780)	0.886 (702)	0.894 (584)	RWB,BWB	FSRQ
PKS B1406–076	0.320 (203)	0.359 (179)	0.348 (221)	0.503 (213)	0.643 (47)	RWB	FSRQ
PKS B1424–418	0.881 (428)	0.903 (425)	0.893 (426)	0.891 (423)	0.911 (412)	RWB	FSRQ
PKS 1510–08	0.410 (598)	0.469 (596)	0.485 (600)	0.599 (588)	0.650 (529)	RWB	FSRQ
PKS 1622–29	0.235 (257)	0.232 (251)	0.296 (276)	0.423 (313)	0.755 (234)	RWB	FSRQ
PKS 1730–13	0.345 (243)	0.297 (226)	0.329 (282)	0.390 (280)	0.502 (211)	RWB	FSRQ
PKS 1954–388	0.320 (47)	–	0.397 (92)	0.588 (94)	–	RWB	FSRQ
2023–07	0.687 (103)	–	0.633 (101)	0.940 (85)	–	RWB	FSRQ
PKS 2052–47	0.600 (208)	0.636 (208)	0.606 (215)	0.705 (223)	0.731 (229)	RWB	FSRQ
PKS 2142–75	0.183 (161)	0.198 (165)	0.215 (196)	0.532 (205)	0.644 (194)	RWB	FSRQ
PKS 2155–304	0.410 (462)	0.400 (460)	0.396 (462)	0.409 (407)	0.507 (398)	No trend	BL Lac
3C 454.3	0.621 (883)	0.651 (849)	0.712 (868)	0.849 (856)	1.020 (689)	RWB	FSRQ
PKS 2326–502	0.845 (169)	–	0.898 (279)	0.950 (139)	0.961 (107)	RWB	FSRQ
PMN J2345–1555	0.646 (91)	–	0.727 (217)	0.664 (214)	0.708 (99)	RWB	FSRQ

Table 3. Mean variability characteristics of the blazars in optical and infrared bands.

Class	*B*	*V*	*R*	*J*	*K*
BL Lac	0.56 ± 0.29	0.62 ± 0.23	0.54 ± 0.25	0.60 ± 0.25	0.69 ± 0.14
FSRQ	0.46 ± 0.26	0.48 ± 0.26	0.51 ± 0.25	0.59 ± 0.24	0.72 ± 0.19

our sample of sources, we generated colour ($B - J$)–magnitude (J-band) diagrams. Linear least squares fit was carried out on the data points in the colour–magnitude diagram by properly taking into account the errors in both colour and magnitude. For this, we used BCES method [2] (Akritas & Bershady 1996; Nemmen et al. 2012) of orthogonal least squares to find the slope and intercept. A positive slope in the colour–magnitude diagram is an indication of a BWB trend, while a negative slope is an indication of a RWB trend. The generated colour–magnitude diagrams for all the objects in our sample, along with the linear least squares fit are given in Figs 5–7. The results of the linear least squares fit to the colour magnitude diagram are given in Table 4. We considered BWB colour–magnitude variation in a source if the Spearman rank correlation coefficient is positive and the probability p of no correlation is lesser than 0.05. Similarly, a source is considered to have shown a RWB trend if values of the Spearman rank correlation coefficient is negative and p is lesser than 0.05. Using the above criteria, we found that a large fraction of the sources in our sample (80 per cent) showed a RWB trend. No spectral change with brightness was noticed in three sources, while another two sources showed a BWB trend. In two sources, namely A0 0235+164 and 3C 379, we noticed both BWB and RWB trend. They showed an RWB trend upto a certain J-band brightness and for magnitudes brighter than that they showed a BWB behaviour. For two sources PKS 0637–75 and BZQ J0850–1213, two deviant point each (shown as purple points in 5 and 6, respectively) were excluded from the fit, as inclusion of those points gave large errors in the derived slope and intercept. These observations indicate that complex spectral

[2] https://github.com/rsnemmen/BCES

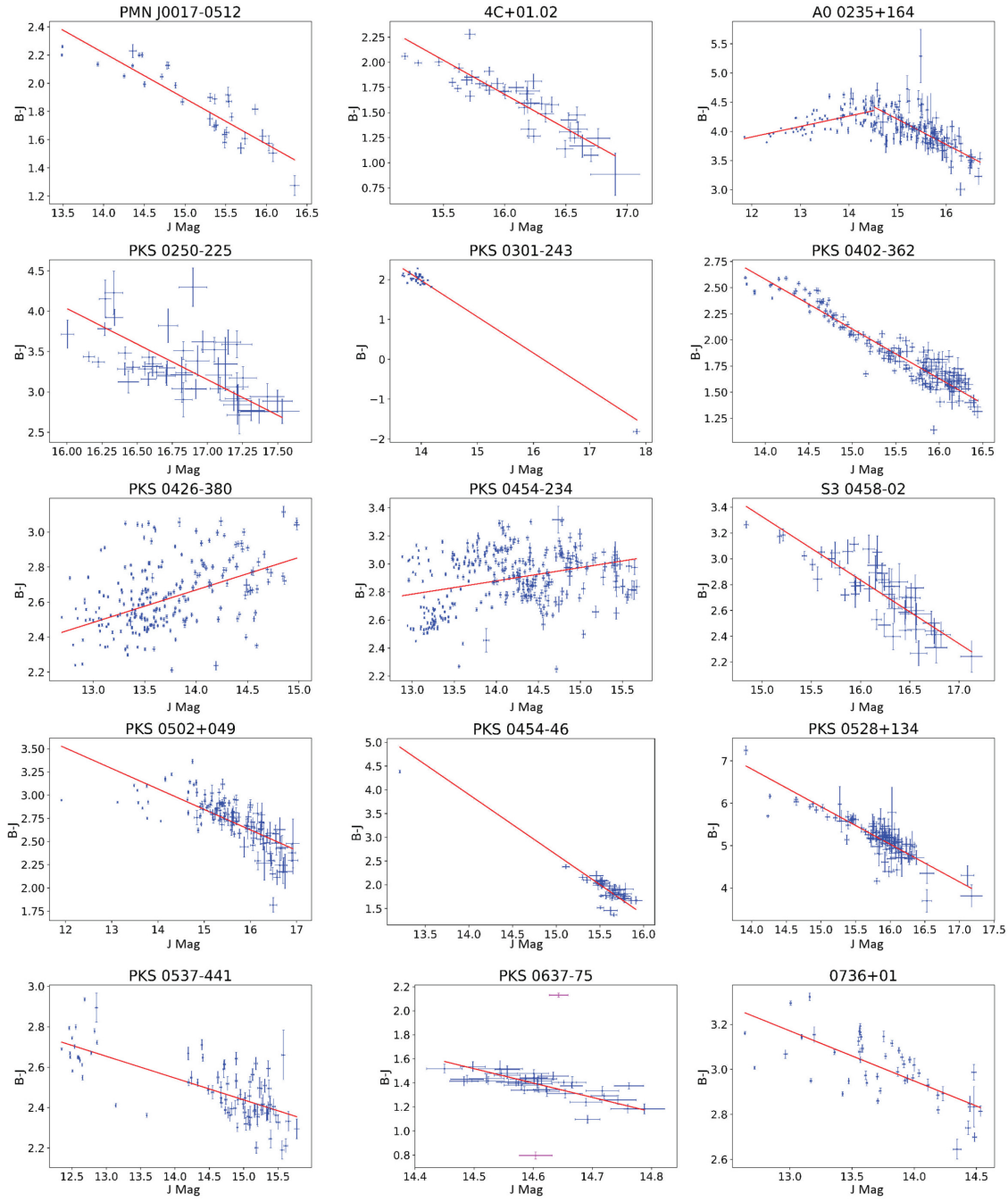

Figure 5. Correlation between $(B - J)$ colour and J-band brightness of the blazars. The solid line is the linear least squares fit to the data. The names of the objects are given on each panels.

variations with brightness are invariably present in FSRQs and BL Lacs.

3.3 Multiwavelength cross-correlation

All the sources analysed in this work are highly variable in both optical and infrared bands. To check for correlation between the flux variations in different bands, we used the discrete correlation function (DCF; Edelson & Krolik 1988; White & Peterson 1994) and the interpolated cross-correlation function (ICCF) techniques (Gaskell & Sparke 1986; Gaskell & Peterson 1987). The DCF method calculates the correlation function from unevenly sampled data. For two light curves, say x_i and y_j, this method calculates a set of unbinned discrete correlation functions (UDCFs) given as

$$\mathrm{UDCF}_{ij} = \frac{(x_i - \overline{x})(y_j - \overline{y})}{\sqrt{\left(\sigma_x^2 - e_x^2\right)\left(\sigma_y^2 - e_y^2\right)}} \quad (4)$$

,here $\overline{x}$ and $\overline{y}$ are the mean of the two light curves, σ_x and σ_y are the standard deviations of the two light curves, and e_x and e_y are the errors in each data point. For any time lag (τ), DCF is taken as the average of all UDCFs having the same τ. Taking the average of M

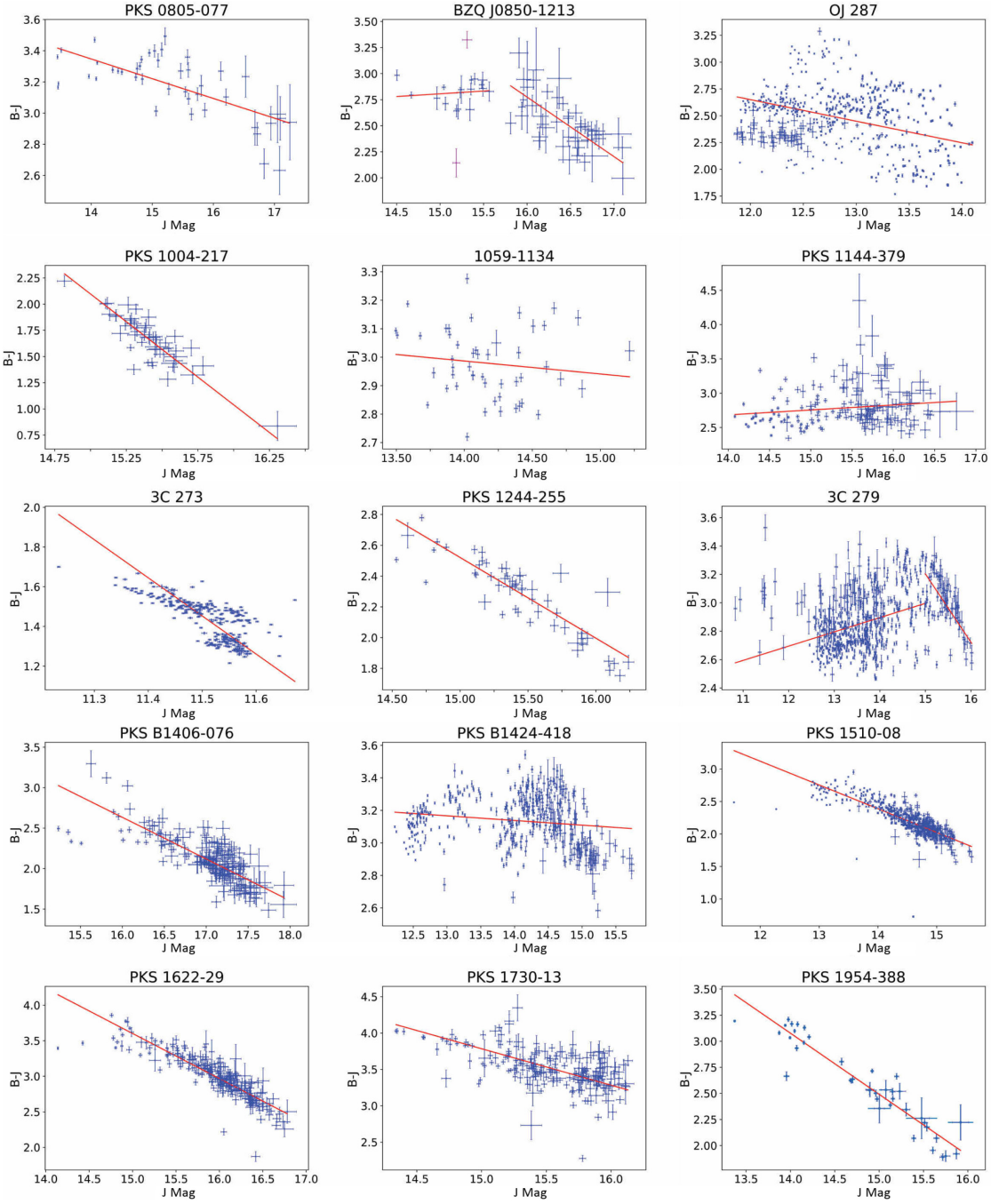

Figure 6. Correlation between $(B - J)$ colour and J-band brightness of the blazars. The solid line is the linear least squares fit to the data. The names of the objects are given on each panels.

pairs of UDCFs for which $\tau - \Delta\tau/2 \leq \Delta\tau_{ij} < \tau + \Delta\tau/2$, we get

$$\mathrm{DCF}(\tau) = \frac{1}{M} \sum \mathrm{UDCF}_{ij}. \quad (5)$$

The error in each DCF bin is given as

$$\sigma(\tau) = \frac{1}{M-1} \sum [\mathrm{UDCF}_{ij} - \mathrm{DCF}(\tau)]^2{}^{1/2}. \quad (6)$$

To estimate the lag, we used the centroid (τ_{cen}) of the CCF defined as

$$\tau_{\mathrm{cen}} = \frac{\sum_i \tau_i \mathrm{CCF}_i}{\sum_i \mathrm{CCF}_i}. \quad (7)$$

For calculating the centroid, we included those points in the CCF that are within 80 per cent of the CCF peak. To get the errors in the CCF, we followed the Monte Carlo approach based on flux randomization (FR) and random subset selection (RSS) outlined in Peterson et al. (1998) that takes into account the time sampling of the light curves and the randomness in the flux measurements. For each pair of light curves using both FR and RSS, we carried out 10 000 iterations and for each iteration, we determined the τ_{cen}. Using these values, we generated the distribution of CCF values. The median of the CCF distribution is taken as the value of the lag. As the distribution of τ_{cen} obtained from 10 000 iterations is non-Gaussian, the upper ($\Delta\tau_{\mathrm{up}}$) and lower ($\Delta\tau_{\mathrm{low}}$) uncertainties in τ_{cen}

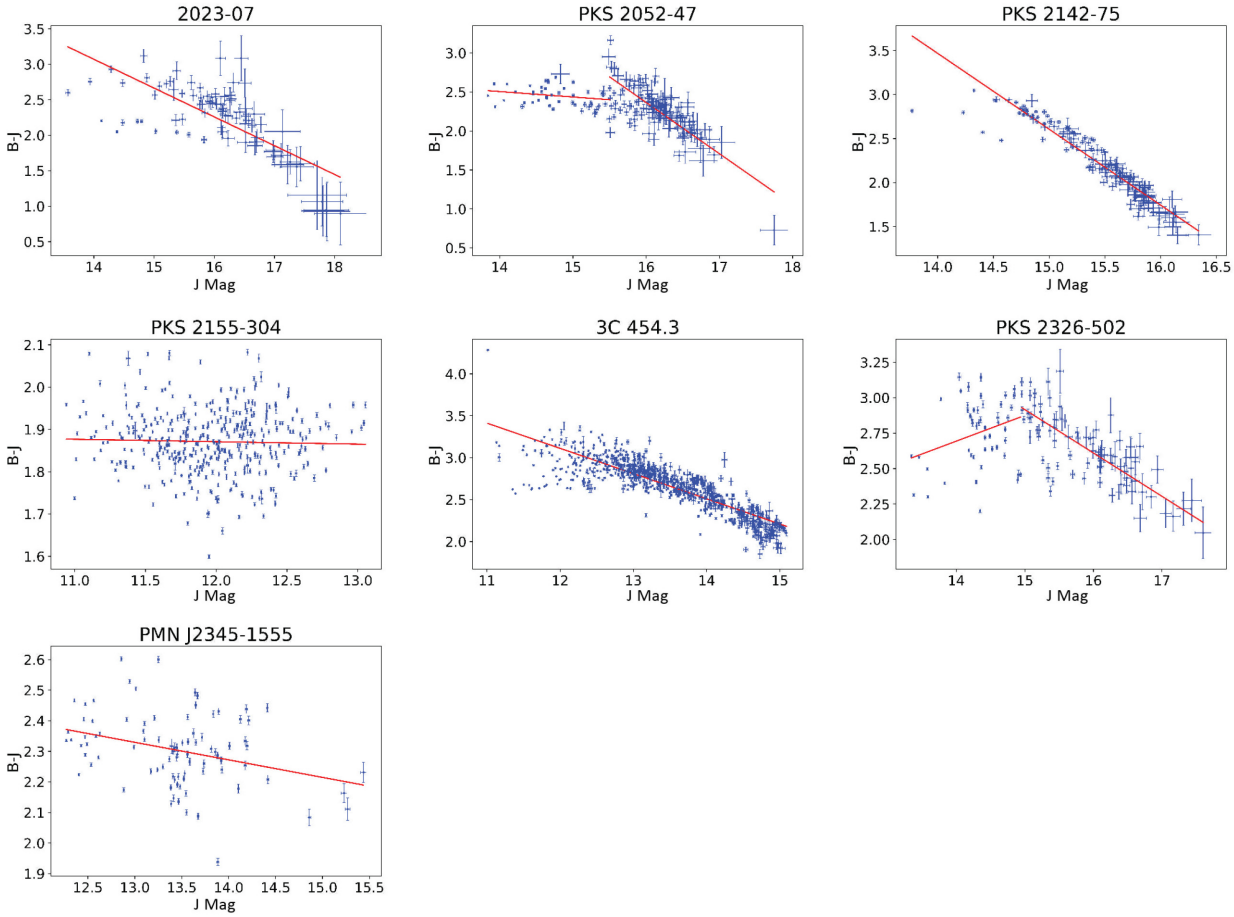

Figure 7. Correlation between $(B - J)$ colour and J-band brightness of the blazars. The solid line is the linear least squares fit to the data. The names of the objects are given on each panels.

were determined such that 15.87 per cent of iterations have $\tau > \tau_{\rm cen} + \Delta\tau_{\rm up}$ and 15.87 per cent of iterations have $\tau < \tau_{\rm cen} - \Delta\tau_{\rm low}$. The upper and lower error thus obtained in $\tau_{\rm cen}$ corresponds to $\pm\, 1\sigma$ for a function that has a Gaussian distribution. The above procedures to obtain the lag and the associated error using DCF method was also repeated using ICCF technique, with the exception that the light curves were first brought to uniform time binning using linear interpolation. Thus, for all the sources, we have two measurements of lag, one using the DCF method and the other one using ICCF method. The cross-correlation plots obtained between B and J bands is shown in Figs 8 and 9. For majority of the sources, we found no lag between the flux variations in B and J bands. Only for three sources, namely, PKS 1144–379 (lag $= 19.3^{+8.9}_{-10.7}$ d), PKS B1424–418 (lag $= 13.4^{+2.0}_{-3.4}$ d), and 3C 273 (lag $= 461.0^{+37.6}_{-30.2}$ d), we found statistically significant lags between flux variations in B and J bands.

4 DISCUSSION

4.1 Flux variability

The long-term optical/*UV* and infrared flux variations observed in blazars could be due to intrinsic processes, extrinsic processes, or a combination of both. Internal physical process includes those related to accretion disc caused by change in accretion rate (Li & Cao 2008) and those related to the relativistic jet such as blobs of emission moving through the helical magnetic fields of the jet (Marscher et al. 2008), the propagation of shock waves in helical jets (Larionov et al. 2013), or changes in the direction and speed of the jet flow (Pollack, Pauls & Wiita 2016). Alternatively, the observed long term flux changes in blazars could also be caused by extrinsic geometrical effects associated with a change in our viewing angle to the moving blob of emission, that leads to variable Doppler boosting of the emitted radiation (Camenzind & Krockenberger 1992; Gopal-Krishna & Wiita 1992; Villata et al. 2009; Larionov, Villata & Raiteri 2010). The observed brightness in the *UV*, optical, and the infrared bands in blazars is a combination of blue thermal emission from the accretion disc and red relativistically beamed non-thermal emission from their relativistic jets (Perlman et al. 2008). The emission from the disc peaks in the *UV* band (the big blue bump at around 3000 Å) and its contribution decreases towards optical and infrared wavelengths. In the infrared band, the thermal emission is thought to come from the dusty molecular torus that reprocesses the photons from the broad-line region and the accretion disc into the infrared region (Antonucci 1993; Perlman et al. 2008). As the thermal emission comes from a larger region in the accretion disc, they are expected to vary less than the variations caused from the jet. The blazars studied here are γ-ray loud sources detected by the *Fermi Gamma-ray Space Telescope* (Ackermann et al. 2015) and are believed to have strong relativistic jets whose non-thermal emission dominates over the thermal accretion disc emission most of the time. Therefore, in this scenario, it is quite natural to expect σ_m to increase with wavelength. This is what is observed on individual sources in

Table 4. Results of the linear least squares fit to the colour magnitude diagram.

Name	Slope	Intercept	R	p
PMN J0017–0512	-0.32 ± 0.03	6.75 ± 0.41	-0.89	4.33×10^{-19}
4C+01.02	-0.68 ± 0.07	12.56 ± 1.12	-0.90	1.31×10^{-14}
AO 0235+164	0.18 ± 0.03	1.75 ± 0.37	0.52	1.11×10^{-06}
	-0.43 ± 0.04	10.73 ± 0.70	-0.69	4.43×10^{-20}
PKS 0250–225	-0.87 ± 0.18	17.91 ± 3.11	-0.61	4.98×10^{-06}
PKS 0301–243	-0.92 ± 0.23	14.86 ± 3.21	-0.48	1.05×10^{-3}
PKS 0402–362	-0.48 ± 0.01	9.24 ± 0.21	-0.92	4.48×10^{-69}
PKS 0426–380	0.19 ± 0.02	0.07 ± 0.28	0.43	7.65×10^{-18}
PKS 0454–234	0.09 ± 0.02	1.55 ± 0.24	0.26	3.11×10^{-06}
S3 0458–02	-0.49 ± 0.04	10.69 ± 0.66	-0.85	5.14×10^{-15}
PKS 0502+049	-0.22 ± 0.03	6.18 ± 0.50	-0.79	2.07×10^{-28}
PKS 0454–46	-1.23 ± 0.36	21.12 ± 5.68	-0.66	1.03×10^{-05}
PKS 0528+134	-0.88 ± 0.08	19.19 ± 1.33	-0.81	1.59×10^{-25}
PKS 0537–441	-0.11 ± 0.01	4.05 ± 0.17	-0.69	1.76×10^{-13}
PKS 0637–75	-1.19 ± 0.23	18.80 ± 3.42	-0.75	4.33×10^{-08}
0736+01	-0.22 ± 0.04	6.06 ± 0.56	-0.68	7.45×10^{-08}
PKS 0805–077	-0.13 ± 0.02	5.13 ± 0.35	-0.65	2.20×10^{-06}
BZQ J0850–1213	0.05 ± 0.14	1.99 ± 2.20	0.30	0.24
	-0.57 ± 0.11	11.94 ± 1.78	-0.67	5.57×10^{-07}
OJ 287	-0.20 ± 0.03	5.08 ± 0.36	-0.24	5.17×10^{-08}
PKS 1004–217	-1.06 ± 0.09	17.96 ± 1.45	-0.81	1.01×10^{-12}
1059–1134	-0.05 ± 0.05	3.62 ± 0.76	-0.16	0.26
PKS 1144–379	0.07 ± 0.04	1.69 ± 0.60	0.12	0.14
3C 273	-1.92 ± 0.11	23.54 ± 1.25	-0.77	1.34×10^{-56}
PKS 1244–255	-0.52 ± 0.05	10.37 ± 0.77	-0.84	3.15×10^{-16}
3C 279	0.10 ± 0.02	1.49 ± 0.24	0.31	3.55×10^{-14}
	-0.48 ± 0.07	10.40 ± 1.12	-0.49	1.49×10^{-06}
PKS B1406–076	-0.51 ± 0.05	10.87 ± 0.85	-0.79	1.48×10^{-40}
PKS B1424–418	-0.03 ± 0.01	3.54 ± 0.12	-0.15	2.54×10^{-03}
PKS 1510–08	-0.37 ± 0.02	7.51 ± 0.24	-0.86	2.64×10^{-167}
PKS 1622–29	-0.63 ± 0.04	13.11 ± 0.64	-0.91	8.20×10^{-92}
PKS 1730–13	-0.50 ± 0.06	11.31 ± 0.87	-0.56	5.51×10^{-19}
PKS 1954–388	-0.59 ± 0.04	11.29 ± 0.58	-0.93	2.33×10^{-18}
2023–07	-0.41 ± 0.06	8.79 ± 0.97	-0.62	2.74×10^{-10}
PKS 2052–47	-0.07 ± 0.06	3.43 ± 0.90	-0.28	6.00×10^{-2}
	-0.66 ± 0.07	12.93 ± 1.21	-0.68	6.49×10^{-19}
PKS 2142–75	-0.86 ± 0.05	12.52 ± 0.72	-0.97	3.87×10^{-86}
PKS 2155–304	-0.01 ± 0.01	1.95 ± 0.11	-0.00	0.98
3C 454.3	-0.30 ± 0.01	6.72 ± 0.13	-0.85	2.63×10^{-233}
PKS 2326–502	0.18 ± 0.14	-0.13 ± 1.98	0.09	0.53
	-0.30 ± 0.02	7.48 ± 0.40	-0.75	5.91×10^{-17}
PMN J2345–1555	-0.06 ± 0.02	3.08 ± 0.21	-0.26	1.49×10^{-2}

this work, where in majority of the objects (about 80 per cent), σ_m in the infrared J and K bands is larger than that in the optical B band irrespective of FSRQs or BL Lacs. Considering FSRQs and BL Lacs as a population, the mean σ_m is found to progressively increase towards longer wavelengths in both FSRQs and BL Lacs (see Table 3) though the standard deviations on each of the mean σ_m values are very large. A two sample KS test was therefore carried out on the distribution of σ_m values between different sets of filters such as (B,R), (R,J), and (B,J) for both FSRQs and BL Lacs. Statistically significant difference was only found between the distribution of σ_m values in B and J bands for FSRQs.

Among blazars, a prominent accretion disc component is mostly seen in FSRQs that have broad emission lines and a radiatively efficient accretion disc relative to BL Lacs that have weak emission lines and radiatively inefficient accretion disc (Ghisellini & Celotti 2001; Ghisellini et al. 2009; Ghisellini 2019). However, it is not always true that accretion disc emission is prominent in FSRQs, as there are instances wherein at increased activity states, the jet emission dominates the accretion disc emission making the accretion disc emission non-distinguishable in the broad-band SED. Similarly, in BL Lacs too there are instances where the strong disc component is prominent in their broad-band SED (Raiteri et al. 2008), particularly during their faint activity states. Irrespective of the conspicuous presence of accretion disc component in the broad-band SEDs of both FSRQs and BL Lacs, the observed optical and infrared emission in most of our sample of γ-ray loud blazars studied here is unambiguously dominated by the red jet emission. Therefore, the increased σ_m towards longer wavelengths seen in majority of the blazars studied here is understood by the dominance of the jet emission in them. Dividing the 37 blazars studied here based on the position of the synchrotron peak in their broad-band SED, we have 33 low synchrotron peaked sources (LSPs), 2 intermediate synchrotron peaked sources (ISPs), and 2 high synchrotron peaked sources (HSPs). In both the ISPs and HSPs too, the amplitude of variability in the infrared J band is found to be larger than the optical B band. Considering the average variability properties of

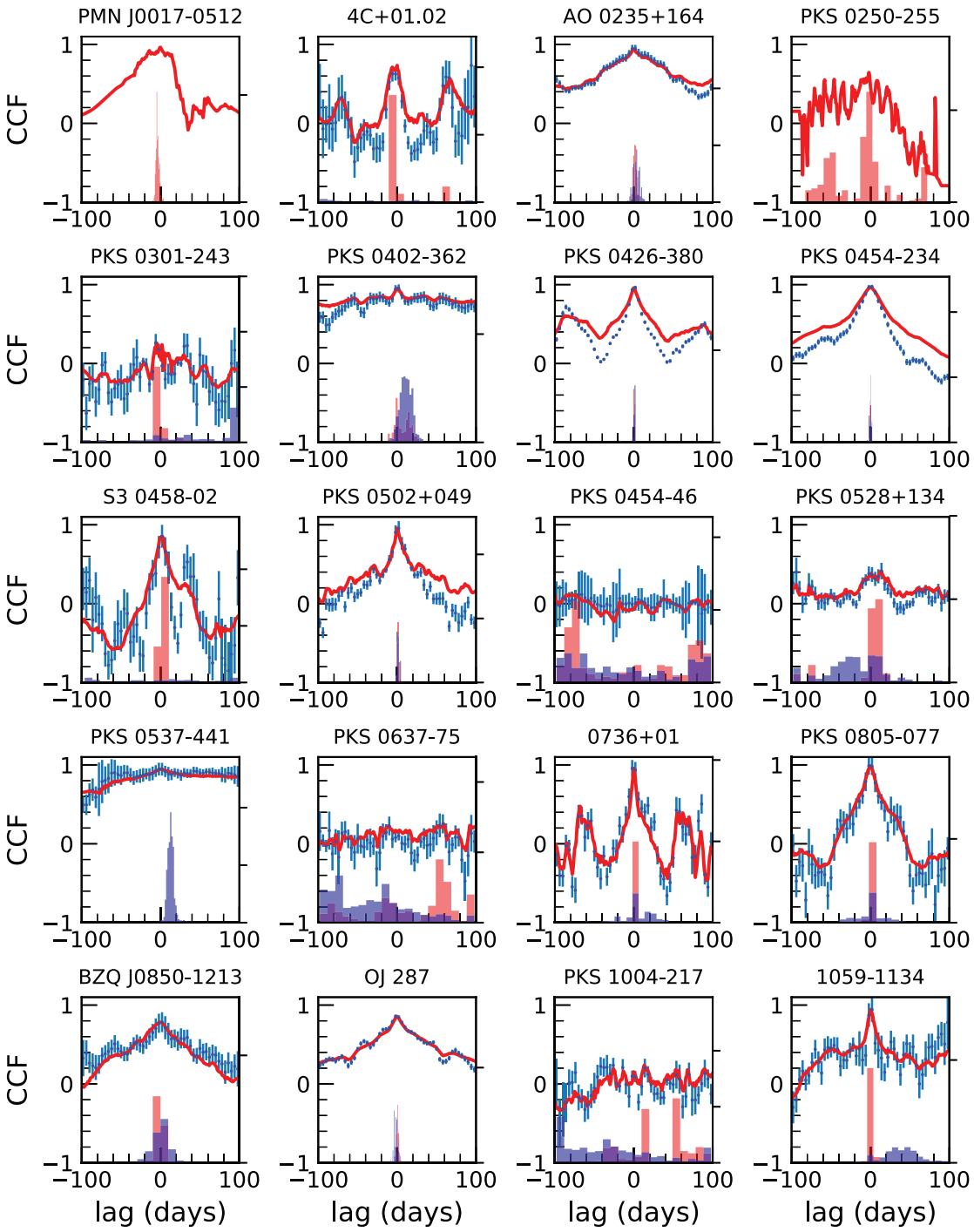

Figure 8. Correlation between the optical *B* band and infrared *J*-band flux variations. The solid lines refer to ICCF, while the blue filled circles with error bars refer to DCF. The distribution of the centroids of the cross-correlation functions are given in blue (ICCF) and orange (DCF), respectively.

the sample of FSRQs and BL Lacs as a whole, we found hints of increased variability amplitude towards longer wavelengths in both the populations which again supports the dominance of jet emission in both the population of blazars. The number of BL Lacs used in this study is only seven, therefore, similar analysis on a large number of FSRQs and BL Lacs are needed to statistically confirm the indications observed from the mean σ_m values shown in Table 3. Considering individual sources in a small fraction of the objects in the sample (that includes FSRQs and BL Lacs), the amplitude of variability is found to increase towards shorter wavelengths (see Table 2) which could be due to the low jet activity of the sources and the emission from the accretion disc becoming prominent over the jet emission.

Based on an analysis of a small sample of blazars utilising data from SMARTS, but spanning only two years Bonning et al. (2012) found FSRQs to show increased variability towards longer wavelengths, while they found BL Lacs not to show larger variability

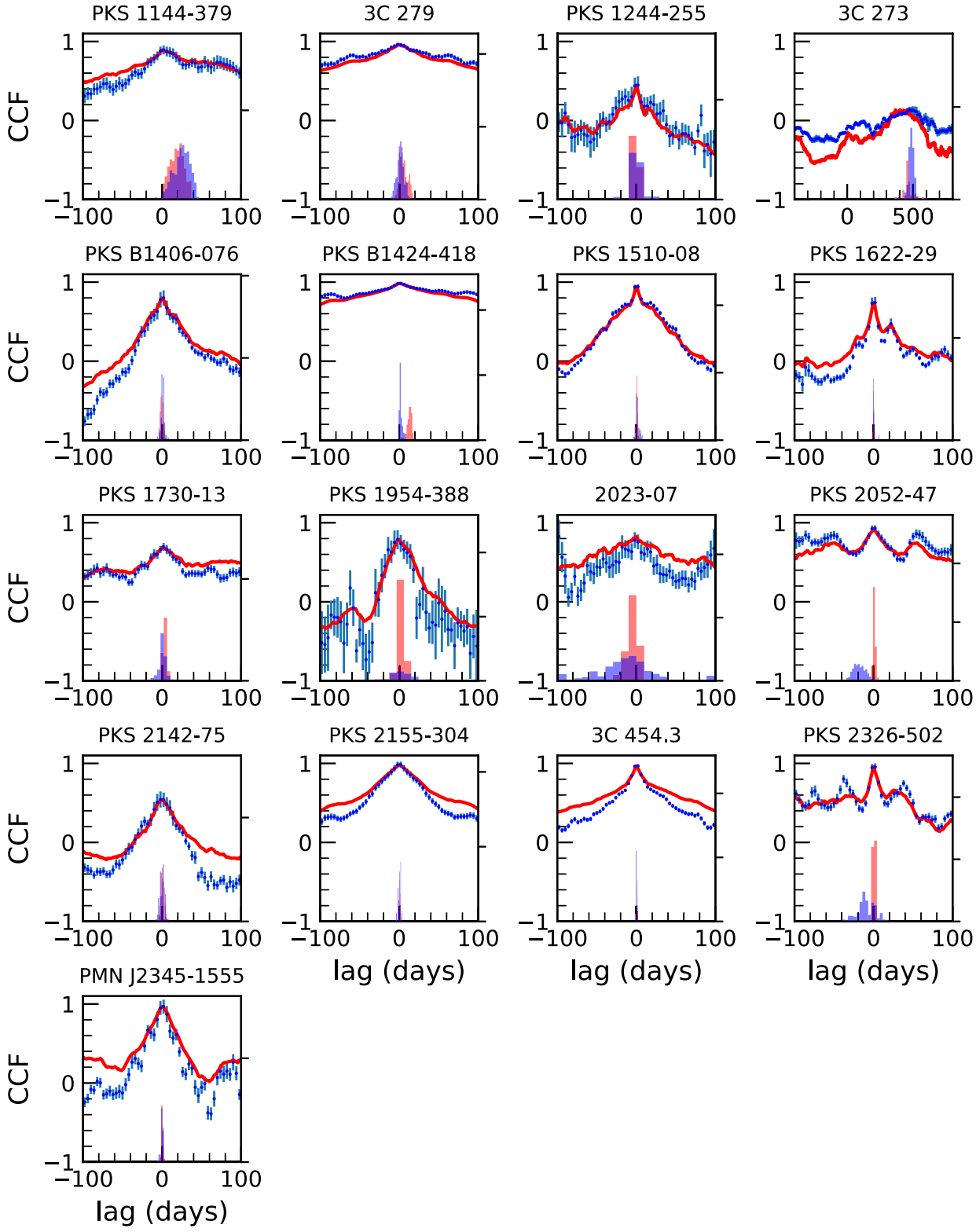

Figure 9. Correlation between the optical *B* band and infrared *J*-band flux variations. The symbols and the distributions have the same meaning as in Fig. 8.

amplitude towards longer wavelengths. Similarly, Zhang et al. (2015) on analysis of a large number of FSRQs and BL Lacs found FSRQs to show larger σ_m in the infrared *J* band relative to the optical *R* band. In the case of BL Lacs, they found the σ_m to be larger in the *R* band relative to *J* band. However, in this work, from an analysis of about 10 yr of data, in a larger number of FSRQs and BL Lacs, we found hints of increased σ_m towards longer wavelengths in both FSRQs and BL Lac, though statistically significant difference was

only found between *B* and *J* bands in FSRQs. Our results for FSRQs are, in general, in agreement with that of Bonning et al. (2012) and Zhang et al. (2015), however, our results on BL Lacs are at odds with what is available in literature (Bonning et al. 2012; Zhang et al. 2015).

Considering the sample of FSRQs and BL Lacs studied in this work as a whole, we found BL Lacs to have larger mean σ_m in all the bands analysed here except *K* band, though the standard deviations in the mean σ_m values are larger. Given the large standard deviation, it is difficult to conclusively say on strong statistical ground that BL Lacs show larger σ_m than FSRQs. Given this caveat, it is likely that both FSRQs and BL Lacs have the same intrinsic jet variability. However, as BL Lacs have small inclination than FSRQs, the difference in the σ_m values of optical and infrared variability between FSRQs and BL Lacs with BL Lacs showing more σ_m compared to FSRQs could be due to BL Lacs viewed at smaller angles than FSRQs and subsequently subjected to higher Doppler boosting. Therefore, the difference in the mean σ_m between FSRQs and BL Lacs found here is in line with what is expected in the unification scheme of radio-loud AGN, but to place the results that are found to be indicative here on a firm footing, this analysis needs to be extended on a large sample of FSRQs and BL Lacs.

4.2 Colour variability

The observed optical, infrared emission in blazars is the sum of the blue thermal emission from the accretion disc and red non-thermal emission from the relativistic jet. The variations seen in the optical and infrared emission from blazars are often accompanied by colour (spectral) variations. Studies of the correlation between colour and brightness variations in blazars can give clues to the relation between accretion disc and jet emission in blazars. However, the correlation between colour and brightness in blazars is highly debated in literature. Reports available in literature indicate that among blazars in BL Lacs, the colour becomes bluer with increasing brightness (BWB; D'Amicis et al. 2002; Vagnetti, Trevese & Nesci 2003; Fiorucci, Ciprini & Tosti 2004; Meng et al. 2018; Gaur et al. 2019), while in FSRQs, the colour becomes redder with increasing brightness (RWB; Bonning et al. 2012; Sarkar et al. 2019). Such a distinct colour–magnitude relation between FSRQs and BL Lacs leads to speculate that the jets of FSRQs and BL Lacs are fundamentally different.

However, in addition to the distinct colour–magnitude relation between FSRQs and BL Lacs, varied colour–magnitude relations too were seen in blazars. For example, in the FSRQ 3C 454.3, BWB trend was observed at certain epochs, while RWB trend was observed at certain other epochs and at one epoch both BWB and RWB trends were observed (Rajput et al. 2019). Also, in another FSRQ, 3C 345, BWB, and RWB trends were simultaneously observed (Wu et al. 2011). In the BL Lac object S5 0716 + 714, Raiteri et al. (2003) found the colour to be weakly correlated with brightness with one clear BWB trend at a certain period, while Stalin et al. (2009) found BWB trend on both inter-night and intra-night time-scales. An RWB trend arises if the relativistic jet emission dominates over the less variable thermal component from the accretion disc (Sarkar et al. 2019). Alternatively, a BWB trend is attributed to increased amplitude of variability at shorter wavelengths (Stalin et al. 2009). Such a scenario, in the one zone synchrotron emission model could happen due to the injection of fresh electrons that have an energy distribution harder than that of the earlier cooler elections, that causes an increase in flux with a BWB trend (Kirk, Rieger & Mastichiadis 1998; Mastichiadis & Kirk 2002). Another explanation for a BWB behaviour is attributed to a change in the Doppler factor (Villata et al. 2004). According to Papadakis, Villata & Raiteri (2007), the BWB colour variation could be due to changes in the Doppler factor, that could happen due to geometrical effects on the variation in the viewing angle of a curved and inhomogeneous jet.

Majority of the sources in our sample showed an RWB trend on analysis of their complete data set. In all such sources, the amplitude of variability in the infrared *J* band is larger than the optical *B* band except three sources, namely PKS 0537–441, PKS 0637–75 and 3C 273. Of these three, PKS 0537–441 is a BL Lac object while the other two are FSRQs. In two sources in our sample, namely A0 0235+164 and 3C 279, we found an RWB trend upto a certain J-band brightness beyond which the spectrum changes shape with increasing brightness. Based on the position of the synchrotron peak of the 37 blazars, 33 are LSP sources, 2 are HSPs, and 2 are ISPs. The RWB trend is invariably found among all the blazar sub-classes as well as among BL Lacs and FSRQs. All the objects studied here are γ-ray emitters and thus have conspicuous jets in them. In this work, we found similar flux and colour variability patterns in both FSRQs and BL Lacs. This leads us to conclude that the jets in both FSRQs and BL Lacs have a similar flux and colour variability behaviour.

5 SUMMARY

We carried out an analysis of the multiwavelength (*BVRJK*) flux variability characteristics of a sample of 37 blazars (that includes 30 FSRQs and 7 BL Lacs) taken from the SMARTS archives using data that spans over 10 yr from 2008–2018. The main findings are summarized below:

(i) All the sources analysed here showed long term flux variations in both the optical and infrared bands. In a majority of the sources (∼80 per cent), the amplitude of variations in the infrared *J* band is larger than the amplitude of variations in the optical *B* band. Considering FSRQs and BL Lacs as a population, there are hints that the amplitude of flux variations in the longer wavelengths is larger than that at the shorter wavelengths. This behaviour is also evident among the different sub-classes of blazars, namely LSP, ISP, and HSP sources. For FSRQs, we found statistically significant difference between the flux variations in *B* and *J* bands. Such increased variations at the longer wavelengths is due to the dominance of the jet emission in blazars.

(ii) Between FSRQs and BL Lacs as a population, the data analysed in this work is suggestive (though statistically insignificant) of BL Lacs showing increased amplitude of flux variations in the optical and infrared bands than FSRQs. This is understood as the jets of BL Lacs are viewed at much smaller angles than FSRQs and thereby subjected to large variability amplitude due to Doppler boosting.

(iii) We found close correlations between colour and brightness changes with a majority of FSRQs and BL Lacs predominantly showing an RWB trend.

(iv) The observed flux and colour variations in this work, lead to conclude that the relativistic jets in FSRQs and BL Lacs are similar.

ACKNOWLEDGEMENTS

We thank the referee for his/her critical comments that helped to improve the manuscript. This paper has made use of up-to-date SMARTS optical/near-infrared light curves that are available at www.astro.yale.edu/smarts/glast/home.php. Safna PZ thanks CHRIST (Deemed to be University) for providing the facilities to carry out

this work. The help by Arun Roy, Ujjwal Krishnan, Sabik PS, Raghu Krishnan, and Shakhil PG is also thankfully acknowledged.

6 DATA AVAILABILITY

The photometric data underlying this article are publicly available from the SMARTS[3] portal.

REFERENCES

Ackermann M. et al., 2015, ApJ, 810, 14
Akritas M. G., Bershady M. A., 1996, ApJ, 470, 706
Angel J. R. P., Stockman H. S., 1980, ARA&A, 18, 321
Antonucci R., 1993, ARA&A, 31, 473
Antonucci R. R. J., 1984, ApJ, 278, 499
Bonning E. et al., 2012, ApJ, 756, 13
Böttcher M., 2007, Ap&SS, 309, 95
Camenzind M., Krockenberger M., 1992, A&A, 255, 59
D'Amicis R., Nesci R., Massaro E., Maesano M., Montagni F., D'Alessio F., 2002, PASA, 19, 111
Dermer C. D., Schlickeiser R., 1993, ApJ, 416, 458
Edelson R. A., Krolik J. H., 1988, ApJ, 333, 646
Fiorucci M., Ciprini S., Tosti G., 2004, A&A, 419, 25
Gaskell C. M., Peterson B. M., 1987, ApJS, 65, 1
Gaskell C. M., Sparke L. S., 1986, ApJ, 305, 175
Gaur H. et al., 2019, MNRAS, 484, 5633
Ghisellini G., 2019, Mem. Soc. Astron. Ital., 90, 6
Ghisellini G., Celotti A., 2001, A&A, 379, L1
Ghisellini G., Maraschi L., Tavecchio F., 2009, MNRAS, 396, L105
Gopal-Krishna, Wiita P. J., 1992, A&A, 259, 109
Jones T. W., O'dell S. L., Stein W. A., 1974, ApJ, 188, 353
Kirk J. G., Rieger F. M., Mastichiadis A., 1998, A&A, 333, 452
Konigl A., 1981, ApJ, 243, 700
Larionov V. M. et al., 2013, ApJ, 768, 40
Larionov V. M., Villata M., Raiteri C. M., 2010, A&A, 510, A93
Li S.-L., Cao X., 2008, MNRAS, 387, L41
Liodakis I., Romani R. W., Filippenko A. V., Kiehlmann S., Max-Moerbeck W., Readhead A. C. S., Zheng W., 2018, MNRAS, 480, 5517
Lynden-Bell D., 1969, Nature, 223, 690
Marscher A. P. et al., 2008, Nature, 452, 966
Mastichiadis A., Kirk J. G., 2002, PASA, 19, 138
Meng N., Zhang X., Wu J., Ma J., Zhou X., 2018, ApJS, 237, 30
Mücke A., Protheroe R. J., 2001, Astropart. Phys., 15, 121
Mücke A., Protheroe R. J., Engel R., Rachen J. P., Stanev T., 2003, Astropart. Phys., 18, 593
Nemmen R. S., Georganopoulos M., Guiriec S., Meyer E. T., Gehrels N., Sambruna R. M., 2012, Sci, 338, 1445
Papadakis I. E., Villata M., Raiteri C. M., 2007, A&A, 470, 857
Perlman E., Addison B., Georganopoulos M., Wingert B., Graff P., 2008, Thermal AGN Signatures in Blazarsp. 9,bves.conf)
Peterson B. M., Wanders I., Horne K., Collier S., Alexander T., Kaspi S., Maoz D., 1998, PASP, 110, 660
Pollack M., Pauls D., Wiita P. J., 2016, ApJ, 820, 12
Raiteri C. M. et al., 2003, A&A, 402, 151
Raiteri C. M. et al., 2008, A&A, 480, 339
Rajput B., Stalin C. S., Sahayanathan S., Rakshit S., Mandal A. K., 2019, MNRAS, 486, 1781
Rakshit S., Stalin C. S., 2017, ApJ, 842, 96
Rakshit S., Stalin C. S., Muneer S., Neha S., Paliya V. S., 2017, ApJ, 835, 275
Rani P., Stalin C. S., Rakshit S., 2017, MNRAS, 466, 3309
Rees M. J., 1984, ARA&A, 22, 471
Sarkar A. et al., 2019, ApJ, 887, 185
Sesar B. et al., 2007, AJ, 134, 2236

[3]http://www.astro.yale.edu/smarts/fermi

Sikora M., Begelman M. C., Rees M. J., 1994, ApJ, 421, 153
Stalin C. S. et al., 2009, MNRAS, 399, 1357
Ulrich M.-H., Maraschi L., Urry C. M., 1997, ARA&A, 35, 445
Urry C. M., Mushotzky R. F., 1982, ApJ, 253, 38
Urry C. M., Padovani P., 1995, PASP, 107, 803
Vagnetti F., Trevese D., Nesci R., 2003, ApJ, 590, 123
Villata M. et al., 2004, A&A, 421, 103
Villata M. et al., 2009, A&A, 501, 455
Wagner S. J., Witzel A., 1995, ARA&A, 33, 163
White R. J., Peterson B. M., 1994, PASP, 106, 879
Wu J., Zhou X., Ma J., Jiang Z., 2011, MNRAS, 418, 1640
Zhang B.-K., Zhou X.-S., Zhao X.-Y., Dai B.-Z., 2015, Res. Astron. Astrophys., 15, 1784

This paper has been typeset from a TEX/LATEX file prepared by the author.